Journal of Engineering Mathematics **32:** 177–194, 1997.

Numerical simulation of separated boundary-layer flow

B. WASISTHO, B. J. GEURTS and J. G. M. KUERTEN
Faculty of Applied Mathematics, J. M. Burgers Centre, University of Twente, P.O. Box 217, 7500 AE Enschede, The Netherlands

Received 18 November 1996; accepted in revised form 17 February 1997

Abstract. The numerical simulation of time-dependent, 2-D compressible boundary-layer flow containing a region of separation is studied. The separation is generated by the introduction of an adverse pressure gradient along the freestream boundary. In order to validate the numerical method, a low Mach-number laminar separation bubble flow is considered, which enables an extensive comparison with incompressible results. The generation of an adverse pressure gradient along the freestream boundary can be realized in various ways. An imposed decelerating flow boundary is compared with a suction technique. The effects of the strength of the pressure gradient and the presence of small upstream perturbations on the separation bubble are also investigated. The time-averaged characteristics of the flow are in good quantitative agreement with incompressible approximate theories predicting the condition for separation. The appearance of self-excited vortex shedding in unperturbed flows under a sufficiently strong adverse pressure gradient is consistent with incompressible flow simulations reported in the literature. The satisfactory result achieved in the calculation of the low-Mach-number flow encourages the application of the numerical method to flows with strong compressibility effects.

Key words: DNS, laminar separation bubble, vortex shedding.

1. Introduction

Direct Numerical Simulation (DNS) of flows involving separation has become of considerable interest in recent years. This is strongly motivated by the increasing need to solve practical fluid dynamics problems frequently occuring in aeronautical and mechanical engineering. Many complex flows contain regions of separation which are too complex for a rigorous theoretical analysis, while laboratory experiments often fail to capture important details of the flow, especially near the wall. Presently, the commonly adopted numerical methods to tackle such complex flows are based on the Reynolds-averaged Navier–Stokes equations (RaNS) or on Large-Eddy Simulation (LES). However, the widely used turbulence models for RaNS are known to be inaccurate if separation occurs; even advanced models such as Reynolds-Stress Models still require considerable research for separated flows ([1], pp. 261–267). Moreover, the subgrid models for LES have up to now only been validated for relatively simple flows and considerable development is necessary to extend systematically the LES method to genuinely complex flows. Thanks to the fast increase in computer capacity, DNS of quite complex flows can play a supporting role in raising the physical insight in these flows and to provide the detailed information which is needed for the validation of turbulence and subgrid models. Moreover, this approach can also serve as a validation of numerical methods in RaNS and LES.

In this paper a numerical method for spatial compressible DNS is developed and tested for flows containing separation regions. While the validity of the method has been assessed previously for relatively simple flows [2], here it is applied to complex cases of separated flows in a low Mach-number regime. A low Mach-number is considered in order to compare

the results with incompressible theory as well as with other numerical studies reported in the literature [3], [4], [5] and [6]. The separation is invoked by an adverse pressure gradient along the upper boundary. The pressure gradient is such that the separated time-averaged shear layer reattaches and forms a laminar separation bubble. The flow may exhibit a strong unsteady behaviour in the form of vortex shedding.

Intensive theoretical and numerical studies have been made on laminar separation bubbles in incompressible flows. Semi-empirical methods to predict separation have been proposed by, among others, Stratford [7] and Thwaites [8]. Dobinga *et al.* [9] presented a method to predict the angle between the wall and the dividing streamline at the separation point. Using direct numerical simulations for incompressible flow, Pauley *et al.* [5] found that, for relatively weak adverse pressure gradients, the separated region builds up into a steady separation bubble. This region grows with increasing adverse pressure gradient, until it reaches a certain critical value at which unsteady separation sets in, characterized by a regular, self-excited vortex shedding. Beyond this critical value the length of the time-averaged bubble decreases with increasing adverse pressure gradient. Furthermore, it was found that the shedding frequency, nondimensionalized by the edge velocity and the boundary-layer momentum thickness at separation, is independent of the Reynolds number and the strength of the pressure gradient [5] and [6]. A criterion for the onset of self-excited vortex shedding was proposed in [5]. The instability of incompressible flows containing a laminar separation bubble has also been investigated numerically, among others, by Maucher and Rist [4] and Alam and Sandham [3]. It was found that, if a small amplitude forcing is introduced upstream of the steady bubble, the separated shear layer strongly amplifies the upstream disturbances. Moreover, a periodic vortex shedding was observed by Alam and Sandham. Increasing the suction strength up to a certain critical level, they also observed self-excited vortex shedding, which is in agreement with Pauley *et al.* In the present work computations of perturbed and unperturbed flows at Mach number 0·2 subjected to various pressure gradients are carried out to verify these findings in low-compressible flows. From this comparison we can appreciate the performance of the developed numerical method which is essentially different from incompressible flow solvers. Apart from the differences in the governing equations and the simulation algorithm, the boundary conditions require a specific treatment, especially along the open boundaries.

In addition to the comparison of the basic flow features, we also investigate the effect of different boundary conditions on the resulting laminar separation bubble. In many comparisons between numerical simulation and experiment, an inviscidly derived suction-blowing boundary condition is used in the numerical calculation to match the pressure distribution of the experiment. This method is used for example by Ripley and Pauley [6] to compare their numerical results with the experiment of Gaster [10]. We could also directly prescribe the normal velocity provided by the experiment. To appreciate the effect of the different procedures of defining the freestream boundary condition, we compare three closely related calculations. In the first calculation, a prescribed pressure distribution is used along the upper boundary. In the second, we use the time-averaged normal velocity on the upper boundary resulting from the first calculation to fix the suction. In the third, a normal velocity distribution is fixed along the upper boundary which is derived from the potential-flow assumption and which matches the prescribed pressure distribution of the first calculation. Finally, we establish the occurrence of spontaneous vortex shedding at sufficiently high adverse pressure gradients.

The paper is organized as follows. In Section 2 we outline the numerical method. Section 3 provides a discussion of the simulation results and finally, we summarize our findings in Section 4.

2. Numerical method

In this section we present the numerical method to solve the mathematical model of the flow. We first present the mathematical model, followed by an outline of the discretization method and a description of the numerical treatment along artificial boundaries.

2.1. GOVERNING EQUATIONS

Unsteady compressible flow over a flat plate is described by the Navier–Stokes equations which represent conservation of mass, momentum and energy:

$$\begin{aligned} &\partial_t \rho + \partial_j(\rho u_j) = 0, \\ &\partial_t(\rho u_i) + \partial_j(\rho u_i u_j) + \partial_i p - \partial_j \tau_{ij} = 0, \\ &\partial_t e + \partial_j((e+p)u_j) - \partial_j(\tau_{ij} u_i - q_j) = 0. \end{aligned} \tag{1}$$

The symbols ∂_t and ∂_j denote the partial differential operators ∂/∂_t and $\partial/\partial x_j$ with respect to time (t) and spatial coordinate (x_j), respectively; ρ is the density, p the pressure, u_i the ith component of the velocity vector, and e the total energy density which is given by:

$$e = \frac{p}{\gamma - 1} + \tfrac{1}{2}\rho u_i u_i, \tag{2}$$

where γ denotes the adiabatic gas constant. Moreover, τ_{ij} is the stress tensor which is a function of the dynamic viscosity μ and velocity vector **u**:

$$\tau_{ij} = \frac{\mu(T)}{\mathrm{Re}}(\partial_j u_i + \partial_i u_j - \tfrac{2}{3}\delta_{ij}\partial_k u_k), \tag{3}$$

where $\mathrm{Re} = (\rho_\infty u_\infty \delta^*)/\mu(T_\infty)$ is the reference Reynolds number. The dynamic viscosity μ can be constant or related to the temperature T by Sutherland's law. Finally, q_j is the viscous heat flux vector, given by

$$q_j = -\frac{\mu}{(\gamma - 1)\mathrm{Re}\ \mathrm{Pr} {M_\infty}^2}\partial_j T, \tag{4}$$

where Pr is the Prandtl number and M_∞ is the reference Mach number. The temperature T is related to the density ρ and the pressure p by the ideal gas law

$$T = \gamma M_\infty^2 \frac{p}{\rho}. \tag{5}$$

Throughout we use $\gamma = 1{\cdot}4$ and $\mathrm{Pr} = 0{\cdot}72$. The values of the reference Mach number M_∞ and the Reynolds number Re are specified for each case separately. The variables have been made dimensionless by reference scales, *i.e.* a reference length δ^* which is taken equal to the displacement thickness of the inflow boundary-layer, density ρ_∞, velocity u_∞, temperature T_∞ and viscosity $\mu(T_\infty)$. The subscript ∞ refers to the freestream value.

The initial condition is specified in two steps. In the first step, we take the full similarity solution to the compressible boundary-layer equations. This implies that, given the compressible Blasius solution at some streamwise location x_1, the solution at a different location $\hat{x}_1$ can be

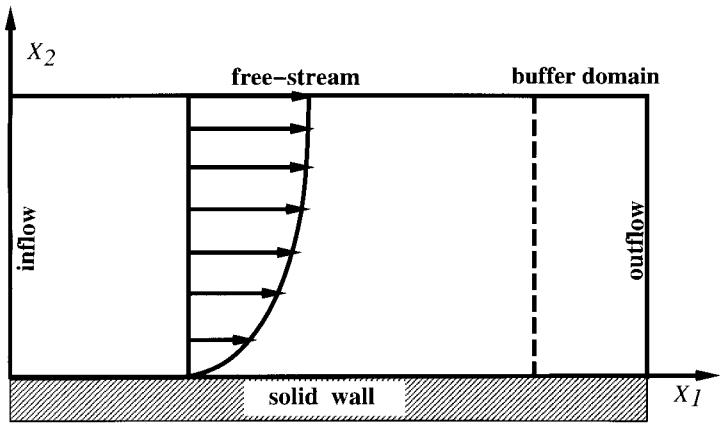

Figure 1. Configuration of the computational domain bounded by a solid wall and open 'artificial' boundaries.

found straightforwardly, provided we scale the normal coordinate by $\hat{x}_2 = x_2\sqrt{\hat{x}_1/x_1}$. Specifically, if ς denotes any component of the solution then $\varsigma(\hat{x}_1,\ (\hat{x}_1/x_1)^{1/2}x_2) = \varsigma(x_1,\ x_2)$. The normal velocity of the compressible Blasius solution is given by ([11], pp. 36):

$$u_2(x_1, x_2) = \frac{1}{(2x_1\mathrm{Re})^{1/2}}\left[u_1(x_1, x_2)\int_0^\eta \tilde{T}(s)\,\mathrm{d}s - T(x_1, x_2)\int_0^\eta \tilde{u}_1(s)\,\mathrm{d}s\right], \tag{6}$$

where η denotes the so called Blasius characteristic length defined as

$$\eta = (\mathrm{Re}/2x_1)^{1/2}\int_0^{x_2} \rho(x_1, s)\,\mathrm{d}s \tag{7}$$

and $\tilde{T}$, $\tilde{u}_1$ denote the temperature and streamwise velocity as functions of the similarity coordinate. In the second step, we scale the similarity solution with the freestream quantities. These quantities are different from the similarity solution, since we apply a nonzero pressure gradient along the freestream boundary. The freestream variables relate to each other according to the isentropic relations.

The flow is simulated in two spatial dimensions and the computational domain is rectangular with the boundaries as shown in Figure 1, where x_1 denotes the streamwise and x_2 the normal direction. A no-slip isothermal boundary condition is imposed at the wall. Specifically, the velocity components vanish, the wall temperature is prescribed and the pressure is extrapolated from the interior points consistent with the approximate auxiliary condition $\partial_2 p = 0$.

2.2. Discretization method

In this subsection, we outline the fourth order spatial discretization method adopted for the compressible Navier–Stokes equations. Specifically, the differential form of these equations can be written in the following conservative formulation:

$$\partial_t U + \partial_j f_j(U) = 0, \tag{8}$$

where the vector U contains the conserved variables $(\rho, \rho u_i, e)^T$ and f_j represents the flux in the x_j-direction, consisting of the inviscid and the viscous contributions. It is important that the

discretization can also be written in conservative form and dissipation and dispersion errors are kept to a minimum. Best suited for this purpose are, for instance, spectral methods and high-order central-difference approximations. Since we perform nonperiodic flow simulations, we favor a finite-difference approach. In this approach, the convective flux in a point (i, j) can be written in the following form,

$$\left(\frac{\partial f}{\partial x}\right)_{i,j} = \sum_{k=-n}^{k=n} w_k g_{i+k,j} \quad \text{with} \quad g_{i,j} = \sum_{k=-n}^{k=n} h_k f_{i,j+k} \tag{9}$$

in which we use $n = 2$. We call w_k differencing weights and h_k averaging weights.

We can determine the weights by imposing certain requirements on the discretization scheme. For instance, the requirement that the difference scheme is exact for a given basis function $m(x_1)$ leads to the linear relation

$$\sum_{k=-2}^{k=2} w_k m(x_{1(i+k)}) = \frac{\partial m}{\partial x_1}(x_{1(i)}) \tag{10}$$

for the differencing weights and the linear relation

$$\sum_{k=-2}^{k=2} h_k m(x_{1(i+k)}) = m(x_{1(i)}) \tag{11}$$

for the averaging weights, respectively. The basis functions used here are polynomials in x_1 when an equidistant grid is used. On a nonequidistant grid, contrary to second-order schemes, maintaining the conservative property is not trivial. In this case the basis functions are chosen in such a way that the methods remain conservative if the ratio $(x_{1(i+1)} - x_{1(i)})/(x_{1(i)} - x_{1(i-1)})$ is independent of i. This leads to

$$(\partial_1 f)_{i,j} = \frac{4}{3}\frac{(s_{i+1,j} - s_{i-1,j})}{(x_{1(i+1)} - x_{1(i-1)})} - \frac{1}{3}\frac{s_{i+2,j} - s_{i-2,j}}{(x_{1(i+2)} - x_{1(i-2)})} \tag{12}$$

with

$$s_{i,j} = \sum_{k=-2}^{k=2} h_k f_{i,j+k} \tag{13}$$

and the averaging weights h_k read:

$$\begin{aligned} h_{-2} &= -\frac{1}{8}\frac{x_{2(j)} - x_{2(j-2)}}{x_{2(j+2)} - x_{2(j-2)}}, \qquad h_2 = -\frac{1}{8}\frac{x_{2(j+2)} - x_{2(j)}}{x_{2(j+2)} - x_{2(j-2)}}, \\ h_{-1} &= \frac{1}{2}\frac{x_{2(j)} - x_{2(j-1)}}{x_{2(j+1)} - x_{2(j-1)}}, \qquad h_1 = \frac{1}{2}\frac{x_{2(j+1)} - x_{2(j)}}{x_{2(j+1)} - x_{2(j-1)}}, \\ h_0 &= \frac{5}{8}. \end{aligned} \tag{14}$$

It should be noted that we carried out the differentiation with respect to x_1 by differencing weights in the x_1-direction and averaging weights in the x_2-direction. This scheme is fourth-order accurate for smooth grids.

The weights for the second-order derivatives of the viscous terms are computed analogously. We treat the second-order derivatives of the viscous terms as the consecutive application of two first-order derivatives, an 'inner' and an 'outer' respectively. Each first-order derivative is approximated by four-point molecules. We calculate the 'inner' derivative $\partial_1^{\text{in}} f$ in the cell-centres $(i+\frac{1}{2}, j+\frac{1}{2})$ by making use of the information on the vertices $[i-1\cdots i+2, j-1\cdots j+2]$, whereas we compute the 'outer' derivative $\partial_1^{\text{out}} f$ in the vertices (i, j) by using the derivatives $\partial_1^{\text{in}} f$ in the cell centres $[i-\frac{3}{2}\cdots i+\frac{3}{2}, j-\frac{3}{2}\cdots j+\frac{3}{2}]$.

The discretization near the boundaries is performed in the same manner as in the interior domain by the creation of dummy points outside the boundaries. Dummy variables are obtained through extrapolation of the interior variables. Second-order and fourth-order extrapolation polynomials are used for, respectively, the second-order and the fourth-order finite-difference schemes, except along the freestream boundary where always second-order extrapolation is employed. Furthermore, no conservation equation needs to be discretized along the wall. The condition $\partial_2 p = 0$ at the wall is discretized to second-order accurate. These boundary treatments maintain adequate accuracy in the spatial discretization near the boundaries. A comparison of this fourth-order discretization scheme and a second-order scheme, which is derived in similar way, shows that the present method performs better in terms of the dissipation and dispersion errors [2].

The time integration is performed by an explicit, second-order accurate, compact-storage, four-stage Runge–Kutta scheme. The grid is uniform in the x_1-direction and stretched in the x_2-direction according to $x_2 = L_2 A y/(1 + A - y)$, where A is a stretching parameter; L_2 denotes the height of the domain and $0 \leqslant y \leqslant 1$, uniformly distributed. In this way the grid becomes more dense towards the wall. The value $A = 0{\cdot}35$ is found to be appropriate for the present flow application.

2.3. Numerical treatments along artificial boundaries

The artificial boundaries are the inflow, freestream and outflow boundaries. At the inflow boundary, the temperature and the inflow velocities are prescribed. In addition, we use a pressure extrapolation from inside the domain, *i.e.* we approximate $\partial_1 p = 0$. This implies

$$T = \hat{T}(x_2, t), \tag{15}$$

$$u_i = \hat{u}_i(x_2, t) \quad \text{for } i = 1, 2, \tag{16}$$

$$p = b_1(x_2)p_1(x_2, t) + b_2(x_2)p_2(x_2, t) + b_3(x_2)p_3(x_2, t), \tag{17}$$

where $p_1, \ldots, p_3$ are the pressures in the first three interior points adjacent to the inflow boundary. The coefficients $b_1, \ldots, b_3$ vary with x_2 in such away that the inflow pressure is zeroth order extrapolated from the interior pressures at the wall and second order extrapolated at the freestream part. Further, $\hat{T}$ and $\hat{u}_i$ describe the behaviour of the temperature and the velocity at the boundary. In time-dependent simulations, these consist of a mean-flow component as described above with small amplitude perturbations following from linear stability theory added. The condition on p allows the pressure at the inflow to vary in response to the disturbances originating from the downstream condition.

Near the outflow boundary the flow is relaxed to a steady base flow in a buffer region, which has a typical length of two to four wave-lengths of the inflow disturbance. Initially, this base flow is taken equal to the similarity solution near the outflow boundary. After a statistically stationary state is reached, a time-averaged solution is employed as the base flow. In the buffer

region the disturbances are reduced to zero directly by multiplication with a specific damping function. This approach can be described as follows,

$$U = U_{\text{ref}} + \zeta(x_1)(\tilde{U} - U_{\text{ref}}), \tag{18}$$

where $U = (\rho,\ \rho u_i,\ e)^T$, U_{ref} is the steady base flow, $\tilde{U}$ is the instantaneous solution and ζ is a damping function. The damping given in (18) is applied at every stage of the Runge–Kutta scheme. The damping function is defined as

$$\zeta = \left[(1 - C_1 x_b^2)\left(1 - \frac{1 - \mathrm{e}^{C_2 {x_b}^2}}{1 - \mathrm{e}^{C_2}}\right)\right]^{C_3 \omega \triangle t} \quad \text{with } 0 \leqslant C_1 < 1,\ C_2 > 0, \tag{19}$$

where x_b is a buffer domain coordinate ranging from 0 to 1, C_1, C_2 and C_3 are tuning parameters, ω is the circular frequency of the inflow disturbance and $\triangle t$ is the time step. The procedure through which this function is developed can be found in [2]. Specifically, the first factor in the square brackets in (19) increases the damping level along the front part of the buffer domain when C_1 is increased. The second factor, on the other hand, reduces the fluctuations rapidly to zero within the rear part of the buffer domain. The higher the value of C_2, the more abrupt the reduction will be. By selecting appropriate values of C_1 and C_2, we can control the reduction rate of the disturbances. Numerical experiments lead to $0 \leqslant C_1 \leqslant 0{\cdot}1$ and $10 \leqslant C_2 \leqslant 20$ being appropriate. The power term is added in order to make the buffer domain procedure insensitive to the number of time steps per disturbance period. This implies that the procedure is directly applicable for various grid densities and flow configurations. A typical value of C_3 used here is around 300. Previously, we showed that this procedure prevents the upstream reflection of disturbances more effectively and efficiently than the commonly used method of increasing the viscosity within the buffer domain [2].

Along the upper boundary, the characteristic method is used to define the boundary conditions [12] and [13]. For two-dimensional flows, four characteristic waves are advected with different speeds. The corresponding wave-amplitude variations $\Lambda_1, \ldots, \Lambda_4$ are defined as

$$\Lambda_1 = \lambda_1 \left(\frac{\partial p}{\partial x_2} - \rho c \frac{\partial u_2}{\partial x_2}\right), \tag{20}$$

$$\Lambda_2 = \lambda_2 \left(c^2 \frac{\partial \rho}{\partial x_2} - \frac{\partial p}{\partial x_2}\right), \tag{21}$$

$$\Lambda_3 = \lambda_3 \frac{\partial u_1}{\partial x_2}, \tag{22}$$

$$\Lambda_4 = \lambda_4 \left(\frac{\partial p}{\partial x_2} + \rho c \frac{\partial u_2}{\partial x_2}\right), \tag{23}$$

where λ_i is the velocity at which the corresponding waves are propagating in the x_2-direction. These velocities are given by:

$$\lambda_1 = u_2 - c, \tag{24}$$

$$\lambda_2 = \lambda_3 \ = \ u_2, \tag{25}$$

$$\lambda_4 = u_2 + c, \tag{26}$$

where c is the speed of sound:

$$c^2 = \gamma p/\rho. \tag{27}$$

In order to define completely the four dependent variables along the freestream boundary, we need to define the amplitude variation of the characteristic waves. In the case of positive normal velocity there are three outgoing waves (waves 2, 3 and 4) and one incoming (wave 1), whereas if the normal velocity is negative, we have one outgoing (wave 4) and three incoming waves (wave 1, 2 and 3), under the assumption that $|u_2| < c$. We calculate the amplitude variations of the outgoing waves, using information from the interior domain, while we fix those of the incoming waves by exterior information using the following relations derived from the one-dimesional Euler equations:

$$\frac{\partial p}{\partial t} + \tfrac{1}{2}(\Lambda_4 + \Lambda_1) = 0, \tag{28}$$

$$\frac{\partial u_2}{\partial t} + \frac{1}{2\rho c}(\Lambda_4 - \Lambda_1) = 0. \tag{29}$$

If we prescribe a constant pressure distribution along the upper boundary, which implies $\partial p/\partial t = 0$ in Equation (28), both positive and negative normal velocity regions can occur.

In the region of positive normal velocity the prescribed pressure acts as the external information to fix the incoming wave, as the amplitude variation of the incoming wave Λ_1 is related to that of the outgoing Λ_4 by Equation (28). On the other hand, in the region of negative normal velocity, the nonreflecting principle is used to provide the additional information to fix the other two incoming waves, which implies that $\Lambda_2 = \Lambda_3 = 0$. The same treatment is applied if we use a suction and blowing boundary condition. In this case $\partial u_2/\partial t = 0$ in Equation (29) and the prescribed normal velocity acts as the external information instead of the pressure. In the suction region the prescribed normal velocity is positive and in the blowing region it is negative.

3. Numerical results

We first present results for a laminar separation-bubble flow induced by prescribing the pressure distribution along the freestream boundary in Section 3.1. The accuracy of the results is verified by comparison with well-known empirical theory and numerical findings in incompressible flow. We carry out analogous calculations, using a corresponding suction boundary condition, in Section 3.2 to study the effect of different realizations of the freestream boundary conditions on the development of the separation bubble. The influence of the strength of the pressure gradient and the presence of imposed upstream disturbances are also studied in Section 3.3.

3.1. Reference simulation: separation by prescribing the pressure

The computation is performed on a grid containing 320×96 cells in the streamwise and the normal direction, respectively. The height of the domain is 30 and the length of the physical domain is 330. The inflow boundary is located at $x_1 = 109$ behind the flat-plate leading edge. The Mach-number is 0·2 and the Reynolds number is 330. These physical parameters are globally comparable with those used by Pauley *et al.* (incompressible with Re ranging

from 400 to 800) and by Alam and Sandham (incompressible with Re = 500). At the inflow boundary a periodic disturbance is superimposed on the compressible Blasius solution which has the following form

$$v = \epsilon \,\text{Real}(\psi(x_2)\ \exp[i(\alpha x_1 - \omega_r t)]), \tag{30}$$

where α is the wave number, ω_r the circular frequency, ϵ the disturbance amplitude and ψ the complex eigenfunction vector. In the present case of spatial simulations α is complex, whereas ω_r is real. The disturbance amplitude ϵ is selected to be 0·001. Using the circular frequency of 0·0594, we find that the eigenvalue provided by the linear stability theory is given by

$$\alpha = \alpha_r + i\alpha_i = 0{\cdot}1640 + i0{\cdot}019687, \tag{31}$$

which is a stable mode. The time development of the dependent variables at a certain point is followed. A statistically stationary solution is reached when each variable fluctuates around a nearly constant value. The sampling of data is then carried out over several disturbance periods. The prescribed pressure distribution along the upper boundary is isentropically related to the following streamwise velocity distribution:

$$u_1(x_1) = \begin{cases} 1 & \text{if } x_{\text{in}} \leqslant x_1 \leqslant x_s, \\ 1 + \frac{1}{2}\Delta u_1 \left(\cos\left(\dfrac{x_1 - x_s}{x_e - x_s}\pi \right) - 1 \right) & \text{if } x_s \leqslant x_1 \leqslant x_e, \\ 1 - \Delta u_1 & \text{if } x_e \leqslant x_1 \leqslant x_{\text{in}} + L_1, \end{cases} \tag{32}$$

where $x_{\text{in}} = 109{\cdot}3$ denotes the streamwise coordinate of the inflow boundary, $x_s = 119{\cdot}3$ and $x_e = 369{\cdot}3$ are the interval boundaries between which the freestream flow is decelerated, and $L_1 = 400$ is the length of the computational domain. The larger the velocity drop Δu_1 the higher the adverse pressure gradient will be. Varying this parameter, we found that $\Delta u_1 = 0{\cdot}10$ corresponds to an almost separated flow. In the following, we present the result for $\Delta u_1 = 0{\cdot}12$, which does lead separation. Figure 2a shows the resulting time-averaged separation bubble, while the prescribed pressure distribution is shown in Figure 2b along with the time-averaged wall pressure distribution. The maximum height of the separation bubble is 1·2 with the height at location x_1 defined as the value of x_2 at which $f(x_1, x_2) \equiv \int_0^{x_2} \rho u_1 \,\mathrm{d}x_2' = 0$. This maximum height is only 20% larger than δ^* at the inflow boundary. Hence, the prescribed pressure gradient can be classified as weak. The center of the recirculation region, which is defined as the position (x_1, x_2) where $f(x_1, x_2)$ is minimal, is located near the reattachment point. The wall pressure distribution deviates notably from the prescribed distribution at the upper boundary. Proceeding downstream in the separation region, we observe that the pressure gradient decreases until the center of the recirculation region is reached, behind which it strongly increases right up to the reattachment point. This strong compression near the reattachment region is also observed by Pauley *et al.* and by Gaster [10].

To verify the separation point condition, we compare our result with some semi-empirical relations.Here, these relations are described in a non-dimensional form. Stratford [7] predicted that separation can be expected if

$$S(x_1) = C_p \left(x_1 \frac{\mathrm{d}C_p}{\mathrm{d}x_1} \right)^2 = 0{\cdot}0104, \tag{33}$$

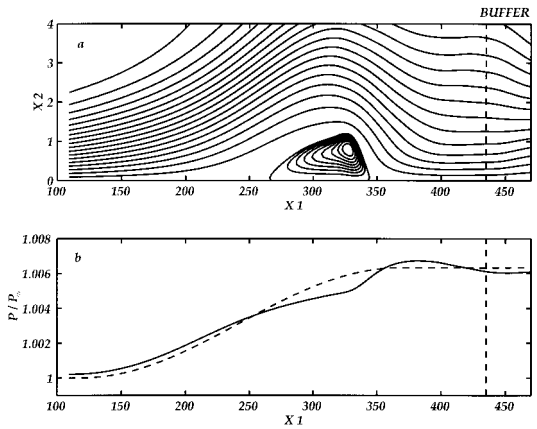

Figure 2. (a) Streamlines of time-averaged bubble due to prescribed pressure, Re = 330 and $M = 0{\cdot}2$. (b) Pressure distribution, prescribed along the upper boundary (dashed) and along the wall (solid).

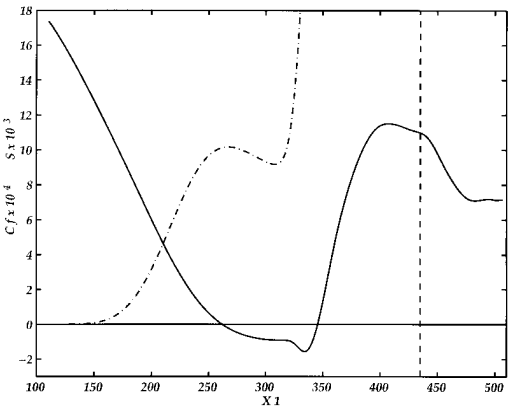

Figure 3. Streamwise variation of skin friction (solid) and Stratford criterion (dashed-dotted).

where

$$C_p = 2(p - p_s)/(\rho u_s^2). \tag{34}$$

The subsript s denotes the location where the adverse pressure gradient starts, equal to x_s in Equation (32). Our result agrees very well with this prediction, as can be seen in the development of the skin-friction c_f which is plotted in Figure 3 along with the value of the Stratford criterion. The value of this criterion based on our result is 0·0101 at the location where $c_f = 0$. We note that the quantities used in calculating the Stratford criterion are averaged over the boundary-layer thickness, since the pressure varies accross the boundary layer. The minimum skin-friction corresponds to the center of the recirculation region. Another method of separation prediction is proposed by Thwaites [8], who found that the value of

$$m = \mathrm{Re}\left[\theta^2 \frac{\partial u_\mathrm{e}}{\partial x_1}\right]_{\mathrm{sep}}, \tag{35}$$

at separation is approximately $-0{\cdot}082$, where u_e denotes the local freestream velocity, θ the momentum thickness of the boundary layer and the subscript sep the separation point. The corresponding value in the present calculation is in the range $-0{\cdot}103 < m < -0{\cdot}065$, depending on the exact definition of the edge velocity u_e in the simulation. This is consistent with values found by Pauley *et al.* ($-0{\cdot}121 < m < -0{\cdot}076$) and by Curle and Skan ($-0{\cdot}171 < m < -0{\cdot}068$) reported in [14]. The slope of the dividing streamline at the separation point is verified against the prediction of Dobinga *et al.* [9]. According to this prediction, the angle between the wall and the dividing streamline is in the range of 0·0588° to 0·0784°. The present result provides a separation angle of 0·0662°, which is within the empirical range. We scrutinize the sensitivity of the result for the grid density by using 64 grid points in the normal direction. We find that the resulting maximum deviations in the boundary-layer integral parameters δ^* and θ are 1·2% and 2%, respectively and, in the maximum height of the separation bubble, 3%.

Next, we check upstream influences of the buffer domain by varying its length. These influences are small, as is illustrated in the development of the disturbance amplitude calculated

with three different buffer lengths in Figure 4a. The results within the domain of interest remain the same. Note that the vertical axis represents the logarithm of the disturbance amplitude. From this figure we observe that the disturbance amplitude is initially damped, which is consistent with the imposed stable mode. The disturbance mode, however, becomes unstable when $\partial_1 p$ at the wall grows, since this gives rise to an inflection point in the streamwise velocity profile [15]. The increase of the disturbance amplitude ends near the recirculation center and the amplitude remains nearly constant further downstream. The corresponding growth rate, which is defined as the derivative of the logarithm of the disturbance amplitude with respect to the streamwise coordinate, is compared with the numerical results of two linear perturbation theories in Figure 4b: linear stability theory (LST) and the linear parabolized stability equations (PSE) (detailed descriptions can be found in [15] and [16], respectively). LST predicts the development of small disturbances in a parallel flow, while PSE can also be used for a nonparallel flow. The prediction of these theories is only valid as long as the disturbances are sufficiently small. As can be seen in Figure 4b, the growth rate of the disturbances from the present calculation agrees well with predictions from LST and PSE up to the beginning of the separation region. Beyond this point the deviation becomes larger as the disturbances increase. From the similarity of the results obtained with LST and PSE, we conclude that the observed deviation is caused by nonlinear effects downstream of the separation point, especially at the position of maximum reverse flow (minimum skin-friction), rather than by the locally parallel assumption of LST. Although we only show the amplitude and the growth rate of the streamwise velocity component, those of the other components behave similarly. The separation region thus acts as an amplifier of the upstream disturbances as suggested by Gaster [10] and Rist and Maucher [4]. We observe, however, that the rate of the amplification strongly decreases behind the center of the time-averaged recirculation region, which is caused by a fast decrease in the strength of the reverse flow. Observing the vortical structure of the flow as shown in Figure 5, we note that periodic vortex shedding occurs near the reattachment region. The shedded vortices are further advected downstream with almost constant thickness at a speed of approximately 40% of the reference velocity. Note that the vortices are damped in the buffer domain. The nearly constant thickness of the vortices corresponds with the almost constant amplitude of disturbances behind the location of vortex shedding. This vortex shedding thus marks a break-down of the laminar boundary layer. By recording the time-oscillation of the dependent variables, we find that the circular shedding frequency is 0·052753, which differs only 0·2% from the imposed perturbation frequency. This suggests that the vortex shedding is directly induced by the Tollmien–Schlichting waves imposed at the inflow boundary.

3.2. Effect of different realisations of the freestream condition

To appreciate the influence of different realizations of the freestream boundary conditions in generating separation, we perform two additional calculations closely corresponding to the case described above, but now using a suction technique. Only the employed freestream boundary conditions are different, the other physical and geometrical parameters remain the same. This suction technique implies that the normal velocity along the upper boundary is prescribed and the other dependent variables are calculated with the characteristic method, as described in Section 2. In the comparison, the previous calculation, which uses the prescribed pressure, is denoted as case A, while the calculations that use the suction technique are denoted as case B and case C. In case B the time-averaged normal velocity along the upper boundary

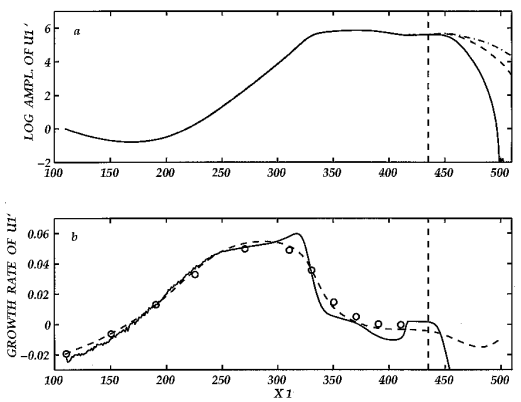

Figure 4. (a) Disturbance amplitude in response of the separation bubble flow calculated with three different buffer lengths normalized by its inflow value. (b) Corresponding growth rate compared with LST (circles) and PSE (dashed).

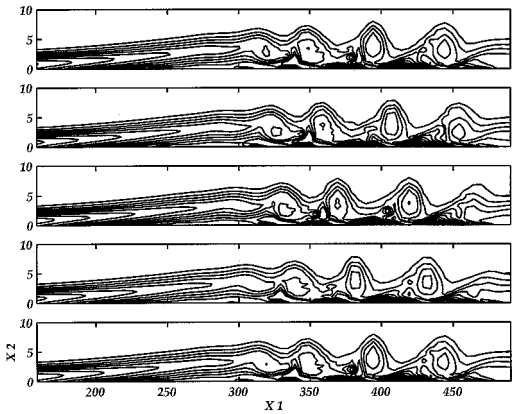

Figure 5. Development of vorticity starting at $t = 603{\cdot}133$ with time interval $26{\cdot}4$.

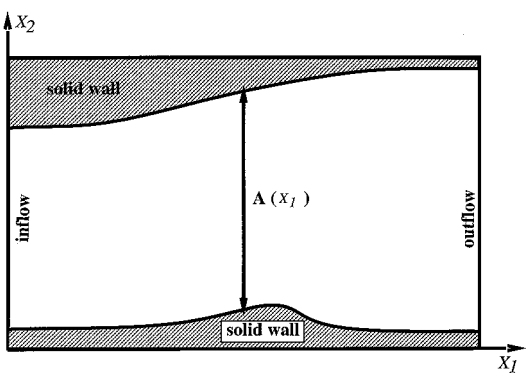

Figure 6. 2-D channel potential flow configuration comparable to a flat-plate viscous flow subjected to suction.

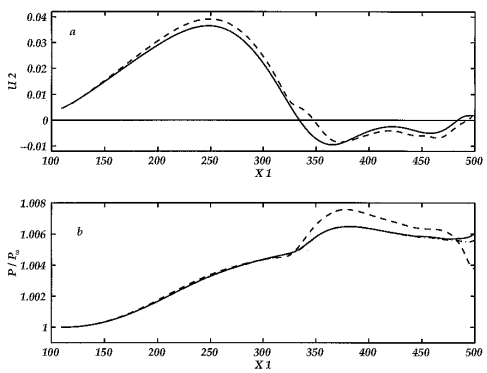

Figure 7. Mean freestream normal velocities (a) and mean wall-pressure distributions (b) corresponding to case A (solid), case B (dashed-dotted) and case C (dashed).

resulting from case A is used as the suction. In case C we derive the suction by assuming incompressible potential flow through a 2D nonuniform channel, as illustrated in Figure 6. The normal velocity along the upper wall defines the suction. The lower wall of this channel is shaped according to the time-averaged displacement thickness δ_1 of case A, in order to take the presence of the boundary layer into account. The channel width A varies according to the streamwise variation of the pressure $\bar{p}$ which is assumed to be constant across the channel width. This pressure distribution $\bar{p}$ is obtained from the mean pressure of case A averaged in the normal direction. We start the derivation of the suction by defining the velocity q along streamlines which corresponds to the pressure distribution $\bar{p}(x_1)$ using the incompressible Bernoulli equation,

$$q = (1 + 2(p_\infty - \bar{p}(x_1)))^{1/2}, \tag{36}$$

where $p_\infty = \gamma^{-1}M^{-2}$ is the undisturbed pressure in the far field. In case A, the maximum normal velocity is small compared to the freestream velocity ($\approx 3{\cdot}5\%$). Therefore, we approximate the streamwise velocity of the channel flow by its streamline velocity $U_1(x_1) \approx q(x_1)$. Recalling that this streamwise velocity is approximately independent of the normal coordinate and using the continuity equation, we find that

$$U_1(x_1)A(x_1) = U_0A_0, \tag{37}$$

where the subscript 0 corresponds to a reference streamwise location. Taking the inflow boundary as this reference point, we relate the channel width $A(x_1)$ to the streamwise velocity $U_1(x_1)$ according to,

$$A(x_1) = \frac{U_0}{U_1(x_1)}A_0. \tag{38}$$

We take $A_0 = 29$, which is different from the height of the computational domain in the DNS in order to take the displacement thickness of the boundary-layer into account. In a potential flow, the slope of the streamline along the wall follows the slope of the wall. Hence,

$$U_2(x_1) = U_1(x_1)\frac{\mathrm{d}}{\mathrm{d}x_1}(A(x_1) + \delta_1(x_1)), \tag{39}$$

where $\delta_1(x_1)$ is the displacement thickness distribution of the boundary-layer in case A and $U_2(x_1)$ the normal velocity along the upper wall. This normal velocity defines the suction along the upper boundary in case C. The time-averaged normal velocity resulting from case A, which is used as the suction in case B, and the prescribed suction in case C are quite similar, as shown in Figure 7a.

The time-averaged quantities resulting from case A and case B are almost the same, whereas the discrepancy between case C and the other two cases is in general only very small up to the separation point, but becomes more pronounced further downstream. This is illustrated for example by the wall pressure and the skin friction of the mean flow in Figure 7b and Figure 8a, respectively. The lines corresponding to case A and case B cannot be distinguished. As case B and case C employ the same suction technique, the slightly larger suction near the reattachment point in case C is the main reason for the deviation in the pressure downstream of the reattachment point. A similar behaviour is also observed in the skin-friction of the time-averaged flows. Due to the larger suction, case C provides a lower minimum skin-friction, representing a stronger reverse flow, and a longer separation region.

The disturbance amplitude in case A is also the same as in case B as shown in Figure 8b. As a consequence of the larger separation region and stronger reverse flow in case C, its disturbance amplitude is slightly higher than in the other cases in the region of separation and further downstream.

From these results we conclude that flows subjected to the pressure boundary condition and the suction boundary condition are equivalent if the freestream pressure in the first case and the freestream normal velocity in the latter case exactly correspond. The difference in the time dependence of the freestream variables (in case A the freestream pressure is steady, while in case B the normal velocity is steady) has apparently a negligible influence. Performing the same comparison for a higher pressure gradient, we found that the equivalence of the two boundary conditions is independent of the pressure gradient.

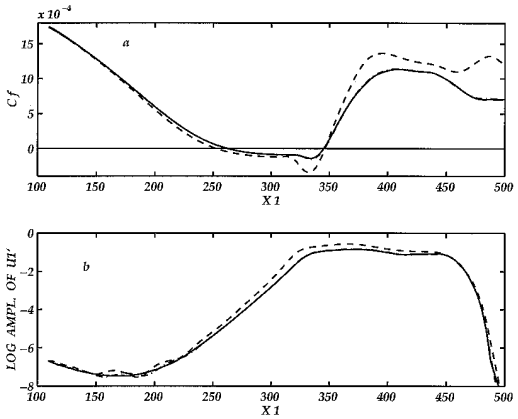

Figure 8. Skin friction (a) and disturbance amplitude (b) for case A (solid), case B (dashed-dotted) and case C (dashed).

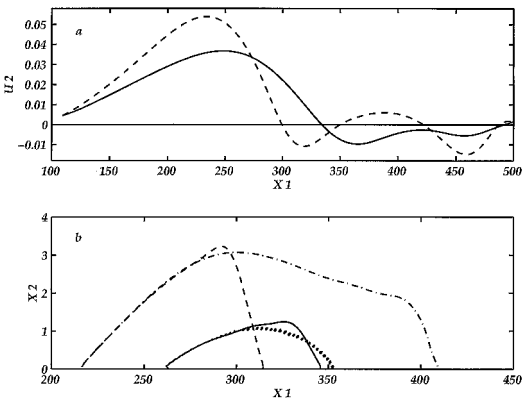

Figure 9. (a) Prescribed freestream normal velocity in case B2 (dashed) and case B (solid). (b) Boundary of separation bubble resulting from case B (solid). B′ (dotted), B2 (dashed) and B2′ (dashed-dotted).

3.3. Effect of pressure gradient and upstream disturbances

In this subsection we investigate the effect of the pressure gradient along the upper boundary on perturbed and unperturbed flows. Therefore, we repeat case B, but without imposing any disturbances, further referred to as case B′, representing an unpertubed flow under a weak adverse pressure gradient. In addition, we perform perturbed (case B2) and unperturbed flow (case B2′) simulations subjected to a stronger adverse pressure gradient realized by a relatively large suction. The suction in case B2, which is also used in case B2′, corresponds to a decelerating freestream flow as described by Equation (32) with $\Delta u_1 = 0{\cdot}16$. Apart from these modifications, the physical flow parameters and the flow configuration are kept the same.

We compute the unperturbed flows, case B′ and case B2′, by removing the imposed disturbances at the inflow boundary. The suction used in cases B2 and B2′ is compared to the freestream normal velocity prescribed in the cases B and B′ in Figure 9a. The time-averaged separation bubbles resulting from the cases B, B′, B2 and B2′ are represented in Figure 9b and the corresponding skin-friction distributions are given in Figure 10. We recall that the length of the region of negative skin-friction represents the length of the separation bubble, while the minimum value of the skin-friction represents the strength of the reverse flow. The comparison shows that a stronger adverse pressure gradient results in a higher separation bubble and a stronger reverse flow independent of whether the flow is perturbed or unperturbed. We note that the reattachment point in case B2′ is quite close to the beginning of the buffer domain. In order to study the influence of the position of the buffer domain on the basic separation process, we repeated the calculation of case B2′ with a different length of the physical domain. This has virtually no influence on the reattachment point. We observed, that the domain of noticeable upstream influence of the buffer is about 30 dimensionless units and is hence strongly localized.

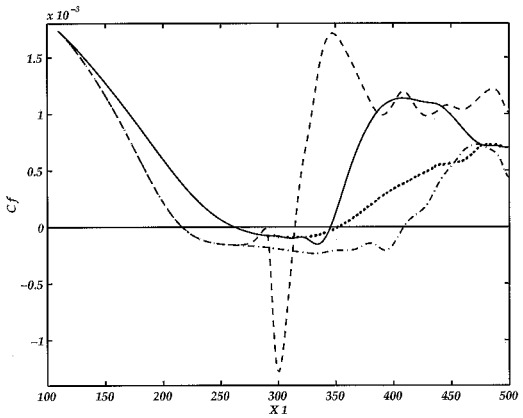

Figure 10. Skin friction resulting from case B (solid), B′ (dotted), B2 (dashed) and B2′ (dashed-dotted).

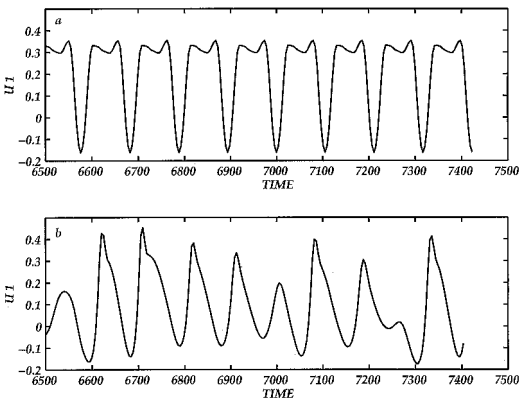

Figure 11. Record of the streamwise velocity in the statistically stationary state near the wall at $x_1 = 430$ in case B2 (a) and in case B2′ (b).

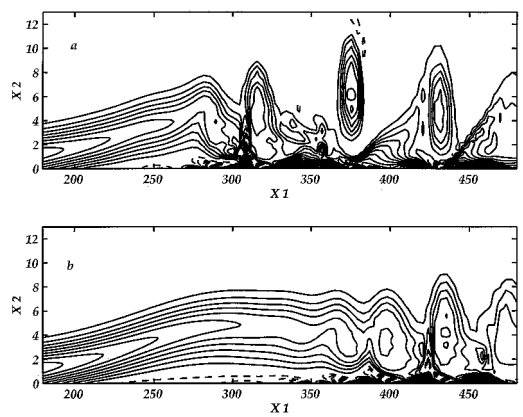

Figure 12. (a) Forced vortex shedding in case B2. (b) Self-excited vortex shedding in case B2′.

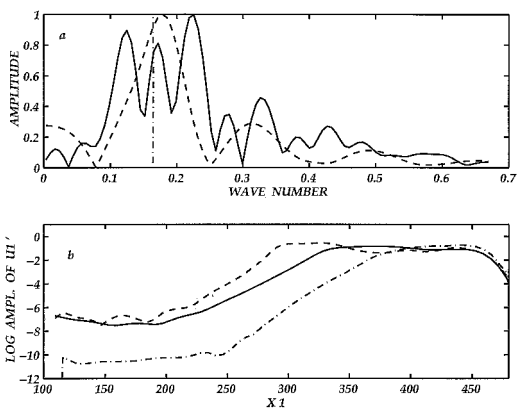

Figure 13. (a) Spectrum of disturbances in case B2 (solid) and case B2′ (dashed). The dashed-dotted line corresponds to the wave number of the imposed disturbances in the perturbed flow. (b) u_1 component disturbance amplitude in case B (solid), case B2 (dashed) and case B2′ (dashed-dotted).

Under the same pressure gradient, the location of the separation point is not affected by the presence of upstream disturbances. However, the unperturbed flows generate longer separation regions and weaker reverse flows than the corresponding perturbed flows. This effect of upstream disturbances is also observed in the incompressible flow simulation of Alam and Sandham. From the present results we note that this upstream perturbation effect is stronger with increasing adverse pressure gradient. We also observe that the recirculation centres of the perturbed flows are located near the reattachment point, while those of the unperturbed flows are near the middle of the separation region.

In case B′ the absence of imposed disturbances results in the disappearance of vortex-shedding such as observed in case B and the instantaneous flow has the same steady character as the time-averaged flow, whereas under the larger suction in case B2′ it gives rise to the occurrence of self-excited vortex shedding. While in case B2 the vortex shedding is periodic

in time, the shedding in case B2′ is irregular. This is illustrated in Figure 11 in which the time development of the streamwise velocity near the wall at $x_1 = 430$ is shown. The shedded vortices in case B2 (forced vortex shedding) are stronger than those in case B2′ (self-excited) as can be seen in Figure 12. Moreover, the vortex shedding in case B2 occurs earlier than in case B2′. The spatial wave number of the disturbances resulting from case B2 and case B2′ is plotted in Figure 13a. The observed three peaks in case B2 correspond, for increasing wave numbers, to the disturbances further downstream of the vortex shedding location, upstream of it and at the location of vortex shedding. In case B2′ the spectrum shows only one dominant wave number which corresponds to the disturbances downstream of the self-excited vortex shedding. The multiple peaks in the spatial wave number in case B2 implies that the propagation velocity of the disturbances is location dependent, since we found that the temporal wave number of the disturbances is independent of location. The lowest propagation velocity is at the location of vortex shedding.

The breakdown of the perturbed laminar shear layer under strong suction (case B2) occurs earlier than under weaker suction (case B), as can be seen in the streamwise velocity disturbance amplitude in Figure 13b. This figure also confirms the earlier breakdown of the perturbed shear layer (case B2), in the form of vortex shedding, compared to the unperturbed one (case B2′). The disturbance amplitudes of other components behave similarly. The different level in the disturbance amplitude in case B2 and case B2′ corresponds to the observed disturbance drop upstream of the reattachment region. Focusing on the region downstream of the inflow boundary in case B2′, we find that the perturbations oscillate with nearly uniform wavelength. This observation, in combination with the disturbance spectrum and the disturbance amplitude development, suggests that the origin of the self-exciting vortex shedding in case B2′ is formed by Tollmien–Schlichting waves. The waves are naturally generated from the existing numerical noise in the flow and their amplitude is enhanced by the strong adverse pressure gradient.

A parameter characterizing the vortex shedding is the so-called Strouhal number, which is defined as the shedding frequency non-dimensionalized by the boundary-layer momentum thickness and the local freestream velocity at the separation point:

$$\mathrm{St}_\theta = f(\theta/u_e)_{\mathrm{sep}}, \tag{40}$$

where f denotes the shedding frequency. Pauley *et al.* [5] suggested that the Strouhal number is independent of Reynolds number and the pressure gradient. The Strouhal numbers deduced from case B2 and B2′ are 0·00672 and 0·00756, respectively. From this we conclude that the presence of small upstream disturbances can affect the Strouhal number, even if the Reynolds number and the pressure gradient are the same.

4. Conclusion

In this paper, a new accurate numerical method is presented that is suitable for DNS of compressible flows involving separation and turbulence.

The results of a low Mach-number laminar separation bubble flow agree well with incompressible-flow results. The condition at the separation point is quantitatively consistent with approximate theories and the features of the flow subjected to different adverse pressure gradients confirm the incompressible results reported in the literature. Specifically, under a weak adverse pressure gradient an unperturbed laminar separation bubble flow

exhibits a steady character, while under a strong adverse pressure gradient it is steady up to the reattachment point, after which a strongly unsteady behaviour in the form of self-excited vortex shedding is found. Under a weak adverse pressure gradient, an unperturbed shear layer exhibits no breakdown. Based on these agreements, we conclude that the compressible-simulation method performs satisfactorily.

We further explore the physical features of the flow, focusing on the effect of different freestream boundary conditions, the magnitude of the adverse pressure gradient and the presence of small upstream disturbances. We investigate two different realizations of a freestream adverse pressure gradient: precribing the pressure and using suction. The time-averaged results which we derived by using the two boundary conditions are the same if the prescribed pressure corresponds exactly with the prescribed normal velocity. This equivalence is independent of the pressure gradient. The potential-flow assumption produces a normal velocity comparable to the normal velocity resulting from the DNS. The results in other quantities are qualitatively the same.

An increase of the adverse pressure gradient results in an earlier occurrence of separation and shear-layer breakdown, a higher separation-bubble, a stronger reverse flow and a larger disturbance amplitude.

If small perturbations are imposed at the inflow boundary, vortex shedding occurs at the end of the separation region for both low and high pressure gradients. The resulting time-averaged bubble is shorter than without small perturbations. The difference in length depends on the applied adverse pressure gradient. Furthermore, under the same adverse pressure gradient forced vortex shedding (perturbed) occurs earlier than self-excited (unperturbed) vortex shedding and the shedded vortices in the first case are stronger. Upstream disturbances also affect the Strouhal number, which is a parameter for the shedding frequency.

We are now investigating an extension of the numerical method to a supersonic laminar separation-bubble flow containing multiple, self-excited, oscillating shocks. The results of this study will be published in the near future.

Acknowledgement

This work is supported financially by the Koninkelijke Nederlandse Academie van Wetenschappen (Royal Netherlands Academy of Sciences, KNAW).

References

1. D.C. Wilcox, *Turbulence Modeling for CFD*. California: DCW (1993) 460 pp.
2. B. Wasistho, B.J. Geurts and J.G.M. Kuerten, Spatial simulation techniques for time-dependent compressible flow over a flat plate. Submitted to *Computers and Fluids* (1996).
3. M. Alam and N.D. Sandham, Simulation of laminar separation bubble instabilities. *Proc. ERCOFTAC workshop on DNS and LES* 1, Grenoble (1996) D.2.1–D.2.10.
4. U. Maucher and U. Rist, Direct numerical simulation of 2-D and 3-D instability waves in laminar separation bubble. *AGARD CP*-551 (1994) 34.1–34.7.
5. L.L. Pauley, P. Moin and W.C. Reynolds, The structure of two-dimensional separation. *J. Fluid Mech.* 220 (1990) 397–411.
6. M.D. Ripley and L.L. Pauley, The unsteady structure of two-dimensional steady laminar separation. *Phys. Fluids A* 5 (1993) 3099–3106.
7. B.S. Stratford, Flow in the laminar boundary layer near separation. *British ARC Report and Memo* 3002 (1954) 1–27.
8. B. Thwaites, Approximate calculation of the laminar boundary layer. *Aero. Q.* 14 (1949) 61–85.
9. E. Dobinga, J.L. Van Ingen and J.W. Kooi, Some research on two-dimensional laminar separation bubbles. *AGARD CP*-4 (1972) 102–110.

10. M. Gaster, The structure and behaviour of laminar separation bubble. *AGARD CP*-4 (1966) 813–854.
11. K. Stewartson, *The Theory of Laminar Boundary Layers in Compressible Fluids*. Oxford: OUP (1964) 191 pp.
12. T.J. Poinsot and S.K. Lele, Boundary conditions for direct simulations of compressible viscous flows. *J. Comp. Phys.* 101 (1992) 104–129.
13. K.W. Thompson, Time dependent boundary conditions for hyperbolic systems. *J. Comp. Phys.* 68 (1987) 1–24.
14. N. Curle and S.W. Skan, Approximate methods for predicting separation properties of laminar boundary layers. *Aero. Q.* 8 (1957) 257–268.
15. L.M. Mack, Boundary layer stability theory. *AGARD Rep.* 709 (1984) (unpublished).
16. F.P. Bertolotti, *Linear and Nonlinear Stability of Boundary Layers with Streamwise Varying Properties*. Dissertation, Ohio State University, Columbus, Ohio (1990) 240 pp.